



Deposited via The University of Leeds.

White Rose Research Online URL for this paper:

<https://eprints.whiterose.ac.uk/id/eprint/173615/>

Version: Accepted Version

---

**Article:**

S'ari, M, Blade, H, Cosgrove, S et al. (2021) Characterization of Amorphous Solid Dispersions and Identification of Low Levels of Crystallinity by Transmission Electron Microscopy. *Molecular Pharmaceutics*, 18 (5). pp. 1905-1919. ISSN: 1543-8384

<https://doi.org/10.1021/acs.molpharmaceut.0c00918>

---

© 2021 American Chemical Society. This is an author produced version of an article published in *Molecular Pharmaceutics*. Uploaded in accordance with the publisher's self-archiving policy.

**Reuse**

Items deposited in White Rose Research Online are protected by copyright, with all rights reserved unless indicated otherwise. They may be downloaded and/or printed for private study, or other acts as permitted by national copyright laws. The publisher or other rights holders may allow further reproduction and re-use of the full text version. This is indicated by the licence information on the White Rose Research Online record for the item.

**Takedown**

If you consider content in White Rose Research Online to be in breach of UK law, please notify us by emailing [eprints@whiterose.ac.uk](mailto:eprints@whiterose.ac.uk) including the URL of the record and the reason for the withdrawal request.

# Characterisation of amorphous solid dispersions and identification of low-levels of crystallinity by Transmission Electron Microscopy

Mark S'ari,<sup>\*,†</sup> Helen Blade,<sup>‡</sup> Stephen Cosgrove,<sup>¶</sup> Rik Drummond-Brydson,<sup>†</sup>  
Nicole Hondow,<sup>†</sup> Leslie P. Hughes,<sup>‡</sup> and Andy Brown<sup>†</sup>

<sup>†</sup>*School of Chemical and Process Engineering, University of Leeds, Leeds, LS2 9JT, United Kingdom*

<sup>‡</sup>*Oral Product Development, Pharmaceutical Technology and Development Operations, AstraZeneca, Macclesfield, SK10 2NA, United Kingdom*

<sup>¶</sup>*New Modalities and Parenterals Development, Pharmaceutical Technology and Development Operations, AstraZeneca, Macclesfield, SK10 2NA, United Kingdom*

E-mail: m.s.s'ari@leeds.ac.uk

## Abstract

Amorphous solid dispersions (ASDs) are used to increase solubility of oral medicines by kinetically stabilising the more soluble amorphous phase of an active pharmaceutical ingredient (API) with a suitable amorphous polymer. Low levels of crystalline material in an ASD can negatively impact the desired dissolution properties of the drug. Characterisation techniques such as powder X-ray diffraction (pXRD), differential scanning calorimetry (DSC) and Fourier transform infrared spectroscopy (FTIR) are often used to detect and measure any crystallinity within ASDs. These techniques are unable to detect or quantify very low levels because they have limits of detection typically

in the order of 1 - 5%. Herein, an ASD of felodipine (FEL) and polyvinylpyrrolidone/vinyl acetate copolymer (PVP/VA) prepared via hot melt extrusion (HME) in a mass ratio of 30:70 was characterised using a range of techniques. No signs of residual crystallinity were found by pXRD, DSC or FTIR. However, transmission electron microscopy (TEM) did identify two areas containing crystals at the edges of milled particles from a total of 55 examined. Both crystalline areas contained Cl- $K\alpha$  X-ray peaks when measured by energy dispersive X-ray (EDX) spectroscopy, confirming the presence of FEL (due to the presence of Cl atoms in FEL and not in PVP/VA). Further analysis was carried out by TEM using conical dark field (DF) imaging of a HME ASD of 50:50 FEL-PVP/VA to provide insights into the recrystallisation process that occurs at the edges of particles during accelerated ageing conditions in an atmosphere of 75% relative humidity. Multiple metastable polymorphs of recrystallised FEL could be identified by selected area electron diffraction (SAED), predominately form II and the more stable form I. Conical DF imaging was also successful in spatially resolving and sizing crystals. This work highlights the potential for TEM based techniques to improve the limit of detection of crystallinity in ASDs while also providing insight into transformation pathways by identifying location, size and form of any crystallisation that might occur on storage. This opens up the possibility of providing enhanced understanding of a drug products stability and performance.

**Keywords:** Amorphous Solid Dispersion, Transmission Electron Microscopy, Organic crystals, Active Pharmaceutical Ingredient, Critical Fluence

## Introduction

Around 90% of drugs in development and 40% of approved drugs in 2010 were classified as having poor aqueous solubility ( $<100 \mu\text{g/mL}$ ) and limited bioavailability when the drug is administered orally.<sup>1,2</sup> This is due to slow, incomplete dissolution of the drug and slow absorption within the gastrointestinal tract. To overcome this challenge, many different approaches have been developed to improve the solubility of active pharmaceutical ingredients (APIs) such as formation of salts, polymeric micelles, nanosuspensions and metastable amorphous phases.<sup>3-6</sup> Amorphous solid dispersions (ASDs) are one of the most successful formulation types that have been used and can be described as a mixture of two or more components in the solid state.<sup>7</sup> They are typically composed of an amorphous API dispersed in a hydrophilic/amphiphilic amorphous polymer matrix. Fusion-based methods (e.g. hot-melt extrusion) and evaporation-based methods (e.g. spray-drying, rotatory evaporation, freeze drying) are often used to intimately mix the API and polymer. Ideally a single homogeneous phase is formed in which the API is molecularly mixed within the polymer matrix to form strong API-polymer interactions.<sup>8</sup> The polymer stabilises the amorphous API phase by inhibiting crystal nucleation or growth and preventing or reducing the rate of amorphous-amorphous phase separation. The amorphous form of an API has a higher, metastable energy state compared to that of the crystalline form and this enhances its solubility and dissolution rate.<sup>9-11</sup> Extremely high API/polymer miscibility and strong molecular interactions are required to form molecular dispersions.<sup>12</sup> For cases where the API and polymer do not mix well at a molecular level, API-rich phases and polymer-rich phases will form. Incomplete or ineffective mixing between the API and polymer can provide sites that initiate recrystallisation either in processing or during storage.<sup>13,14</sup> A lack of stability will reduce the dissolution performance, hindering the use of ASDs.

Solid-state characterisation techniques such as powder X-ray diffraction (pXRD), Fourier transform infra-red spectroscopy (FTIR), differential scanning calorimetry (DSC), polarised light microscopy (PLM) and nuclear magnetic resonance (NMR) spectroscopy are regularly

used to measure re-crystallisation within ASDs as well as for exploring mixing and chemical interactions between the API and polymer.<sup>15</sup> The detection limit for crystalline material in pXRD is approximately 5% by volume, depending on the API, while for DSC residual crystallinity has been measured at around 1% by mass.<sup>16,17</sup> Transmission electron microscopy (TEM) provides high spatial resolution imaging and has recently emerged as a useful analytical technique to study ASDs. Electron diffraction and atomic lattice imaging can detect very localised and low volumes of crystallinity, rather than bulk, and also can be used to identify different polymorphic forms.<sup>18-20</sup> In addition, scanning TEM coupled to energy dispersive X-ray spectroscopy (EDX) and electron energy loss spectroscopy (EELS) can be used to examine API-polymer miscibility or phase separation in ASDs.<sup>21,22</sup> However, TEM is a potentially destructive technique, especially for organic compounds, and the amount of electrons that are absorbed by the sample (the electron dose) must be controlled to ensure the sample is not significantly altered during analysis. Irradiation of the sample by the high energy (1 - 300 keV) electron beam produces secondary electrons that in turn generate free radicals and ions. These highly reactive species cause bond breakage known as radiolysis and this is generally considered to be the main mechanism of electron beam-induced damage in organic compounds.<sup>23-26</sup> A breakdown of chemical bonds then leads to changes in structure, composition and chemistry. For crystalline samples, a loss of crystalline order results in the fading of diffraction spots and a transition to broad, amorphous diffraction rings.<sup>27-29</sup> The electron radiation sensitivity of a crystalline compound can be quantified by measuring the characteristic or critical electron fluence ( $C_F$ ) for the exponential fading of diffraction spots. For example,  $C_F$  have been measured previously by TEM selected area electron diffraction (SAED) for 20 different poorly water-soluble APIs.<sup>29</sup> Knowing the  $C_F$  of a compound provides an electron dose budget to work within for accurate TEM imaging and analysis.

Previous studies involving TEM and pharmaceuticals have employed several different TEM techniques. Ricarte et al. (2015) used dark-field (DF) TEM imaging to detect crys-

tallinity of griseofulvin/hydroxypropylmethylcellulose acetate succinate (HPMCAS) ASDs at a higher sensitivity than modulated DSC and laboratory-scale wide-angle X-ray scattering.<sup>18</sup> Nanocrystalline domains and defects within indomethacin-polyvinylpyrrolidone/vinyl acetate copolymer (PVP/VA) ASDs have been identified using 2D fast Fourier transform analysis of atomic lattice imaging acquired by TEM.<sup>19,20</sup> TEM-EDX has been used to evaluate the difference in composition of phase separated domains in ASDs of evacetrapib-PVP/VA prepared at 50:50 and 90:10 drug loading levels when stored at 97% and 18% relative humidity, respectively.<sup>21</sup> Ricarte et al. (2016) used both conventional TEM-EELS and scanning TEM-EELS on a variety of ASDs prepared by spin-coating different APIs containing aromatic rings and the polymer HPMCAS (which contains no aromatic rings). They demonstrated that the  $\pi - \pi^*$  transition visible in the low-loss region of the EELS spectra could be used for compositional quantification at a sub 100 nm spatial resolution.<sup>22</sup> More recent work by Das et al. (2020) used high resolution monochromated EELS to study several organic compounds in crystalline and amorphous forms.<sup>30</sup> In addition to conventional TEM, scanning transmission electron microscopy (STEM) has been used to analyse lattice defects within crystalline APIs; scanning moiré fringe imaging, allows reproduction of atomic lattice fringes at much lower electron doses than would be required for direct lattice imaging.<sup>31,32</sup> Scanning probe or 4D-STEM has been applied to examine the nanostructure of a paracetamol-theophylline co-crystal and various peptides using low electron fluences of 1 - 5  $e^-/\text{\AA}^2$ .<sup>33,34</sup>

In conjunction with the development of TEM for the analysis of APIs there have been numerous studies investigating the bioavailability of the poorly soluble drug felodipine (FEL) when formulated into various ASDs.<sup>15,35-45</sup> Felodipine is therefore a good candidate to use as a model system to further develop the TEM method. It is a calcium channel blocker and is prescribed to treat hypertension. There are four known polymorphs of FEL and crystallographic information for each polymorph is shown in Table 1. In ambient conditions form I is used in the drug formulations and has been measured as the most thermody-

Table 1: Crystallographic data for FEL polymorphic forms I-IV and their Cambridge Crystallographic Data Centre (CCDC) reference.<sup>46</sup>

	<b>Form I</b>	<b>Form II</b>	<b>Form III</b>	<b>Form IV</b>
Crystal system	monoclinic	monoclinic	monoclinic	monoclinic
Space Group	$P2_1/c$	$C2/c$	$P2_1/n$	$P2_1/n$
a (Å)	12.09	32.39	15.13	11.11
b (Å)	12.08	18.72	7.230	12.57
c (Å)	13.43	23.77	17.28	13.50
$\alpha$ (°)	90	90	90	90
$\beta$ (°)	116.1	91.0	110.2	107.0
$\gamma$ (°)	90	90	90	90
Volume (Å <sup>3</sup> )	1759.3	14373	1773.5	1802.7
CCDC Reference	DONTIJ	DONTIJ01	864026	864027

namically stable polymorph.<sup>46</sup> Form III and then form II are progressively less stable than form I. Less information is available on form IV due to problems with the reproducibility of experiments used to obtain isolated single crystals, although some studies have demonstrated more reliable methods in obtaining crystals of form IV.<sup>47</sup> Polarised light microscopy of the amorphous form has shown it to recrystallise within 5 days without stabilisation by an appropriate polymer.<sup>48</sup> The length of time that a polymer provides stabilisation of the amorphous form depends on the drug loading levels, storage conditions, intermolecular bonding and miscibility between the API and polymer. A study by Luebbert and Sadowski (2017) used pXRD to monitor the long-term stability of ASDs prepared via spray-drying FEL with either polyvinylpyrrolidone (PVP), PVP/VA and polyvinyl acetate (PVAC) at different relative humidity and drug loadings. Here they found that at drug loading levels of 90%, stored at 40°C and 75% relative humidity FEL recrystallised before days 10, 9 and 6 for PVP, PVP/VA and PVAC, respectively. While at a lower drug loading of only 10%, recrystallisation occurred before days 42 and 153 for PVP and PVP/VA respectively, while PVAC remained amorphous during the full 650 days of the study.<sup>49</sup>

Herein we report on a comparison between pXRD, FTIR, DSC and TEM derived measures of crystallisation in ASDs of FEL-PVP/VA prepared in a mass ratio of 30:70 by hot melt extrusion (HME). DF TEM imaging and diffraction were also used to analyse the recrystallisation of a 50:50 w/w FEL-PVP/VA ASD, stored under accelerated ageing conditions

in an atmosphere of 75% relative humidity. We show that TEM analysis can provide an improvement to the limit of detection for crystalline material within an ASD. We then outline how TEM techniques can be used to identify recrystallisation occurrence, location and structural form in an aged dispersion. We also discuss the potential for TEM and advanced scanning techniques to provide a more easily quantifiable measure of crystallisation.

# Materials and Methods

## Hot-Melt Extrusion

Already prepared amorphous solid dispersions (ASDs) of felodipine (FEL) and polyvinylpyrrolidone/vinyl acetate copolymer (PVP/VA) were provided by the AstraZeneca based co-authors. Amorphous solid dispersions of FEL-PVP/VA in mass ratios of 30:70 and 50:50 were prepared by hot-melt extrusion (HME). Components were weighed on an analytical balance and added to a small sterilin pot. The API and polymer were then blended in a Turbula blender at 23 rpm for 4 minutes. Extrusion was carried out on a Thermofisher Haake Minilab II hot-melt extruder using a barrel temperature and screw speed of 130°C and 30 rpm, respectively. The extrudate exited the extruder as long rods approximately 2 mm in diameter, which were cut into smaller sections and milled to form a powder. Each powder was then dried under vacuum and stored at room temperature in a desiccator prior to use.

## Ageing Study

A solid dispersion of 50:50 w/w FEL-PVP/VA was stored at a relative humidity of 75% by placing in a humidity chamber containing a saturated salt solution of KCl inside a desiccator.<sup>50</sup> The relative humidity was measured using a hygrometer within the humidity chamber. The temperature was not controlled or closely monitored but was assumed to remain at approximately 20°C. Before conducting the ageing study the sample was checked for crystallinity by pXRD and TEM.

## Powder X-ray Diffraction (pXRD)

Each sample was mounted onto a silicon wafer and analysed using a PANalytical CubiX PRO diffractometer ( $\lambda = 1.5418 \text{ \AA}$ ). Samples were measured in reflection geometry in a  $\theta - 2\theta$  configuration over a  $2\theta$  scan range of 2° to 40° with a 25 second exposure per 0.02° increment. The X-rays were generated by a copper, long-fine focus tube operated at 45

kV and 40 mA. The samples were spun at 30 rpm to improve counting statistics. Powder diffraction patterns were collected to check for bulk crystallinity and to determine how the crystallinity changed over time. The percentage crystallinity of the aged ASDs was calculated for each diffractogram using Equation 1.<sup>51,52</sup>

$$\% \text{ Crystallinity} = \frac{A_c}{A_c + A_a} \times 100 \quad (1)$$

Here  $A_c$  is the total area under each crystalline, diffraction peak and  $A_a$  is the total area under the amorphous regions.  $A_c$  and  $A_a$  were determined using the software HighScore Plus by manually removing the background and fitting two amorphous peaks using a pseudo-Voigt function. The visible crystalline peaks on top of the amorphous peaks were then each fitted using a pseudo-Voigt function and the total area under the amorphous and crystalline peaks was used to calculate percentage crystallinity using Equation 1.

## **Fourier Transform Infrared (FTIR) Spectroscopy**

A Thermo Scientific Nicolet™ iSTM FTIR ATR spectrometer was used to acquire all the FTIR spectra. Samples were placed onto the ATR crystal and pressed down using a clamp to provide good contact between the sample and crystal. Backgrounds were collected every 15 minutes and the spectra were obtained in % transmission mode from 600 to 4000  $\text{cm}^{-1}$  at a resolution of 2  $\text{cm}^{-1}$ . Data collection was repeated in triplicate for each sample. During analysis, the % transmission was converted to absorbance to increase the ease of identifying weak signals in the presence of much stronger signals.

## **Differential Scanning Calorimetry (DSC)**

A Mettler Toledo DSC was used to collect all calorimetry data. Approximately 10 mg of sample was added to a 100  $\mu\text{L}$  aluminium pan that was then hermetically sealed. An empty aluminium 100  $\mu\text{L}$  pan was used as a reference. Samples were heated from 30 to 200°C

and then cooled back to 30°C under a nitrogen atmosphere at a temperature ramp rate of 10°C/min. Data collection was repeated in triplicate for each sample. Measurements to determine melting temperatures plus the onset and midpoint of the glass transition temperature ( $T_g$ ) of the extruded dispersions was carried out using the Mettler STARe evaluation software.

## **Transmission Electron Microscopy (TEM)**

For TEM analysis, each milled sample was prepared by grinding the dry powder in a pestle and mortar to further reduce the size of the particles. This powder was then attached to a 400 mesh continuous carbon-coated, copper grid by gently touching the powder onto the grid. This was done to avoid any artefacts that would result from dispersing the powder in a solvent. All samples were examined in a Tecnai F20 TEM/STEM operated at an accelerating voltage of 200 kV, and equipped with a field emission gun operating at an extraction voltage of 4.5 kV. The electron flux, which is the rate of electrons passing through the sample per unit area, was controlled by altering the C1 condenser lens by selecting different spot sizes (generally between 7 and 9), and by defocusing the C2 condenser lens to lower the intensity of the electron beam impinging on the specimen. More details on how the electron flux was measured are described in S'ari et al. (2018).<sup>29</sup> Images were captured using a Gatan Orius CCD camera with an exposure time of 2 - 3 seconds to enhance the signal to noise ratio. Energy dispersive X-ray (EDX) spectra were collected using an Oxford Instruments 80mm<sup>2</sup> X-Max silicon drift detector and processed using the AZtec software.

In order to provide statistical analysis of the number of areas found to be crystalline or amorphous 55 different areas of the 30:70 w/w FEL-PVP/VA ASD sample were imaged. To limit any beam-induced damage, only areas not previously exposed to the electron beam were examined at an electron flux between 0.014 and 0.023 e<sup>-</sup>/(Å<sup>2</sup> s). The critical fluence ( $C_F$ ) of FEL has previously been measured by electron diffraction to be  $2.1 \pm 0.9$  e<sup>-</sup>/Å<sup>2</sup>.<sup>29</sup> At this electron flux each sample had approximately 60 - 150 seconds of electron beam exposure

before  $C_F$  was reached.

Selected area electron diffraction (SAED) was used to identify crystalline regions from a selected area aperture diameter of  $1.1\ \mu\text{m}$  at the image plane of a thin sample. The diffraction patterns were aligned and focused prior to acquisition from regions of interest by adjusting focus and centring the zero order spot diffraction on the CCD using a sacrificial piece of specimen. The beam stop was inserted so that the zero order diffraction spot would be blocked when exciting the diffraction lens on an area of interest. Provided the sample had not damaged excessively, dark field (DF) images were collected by inserting a  $2.9\ \text{mrad}$  semi-angle objective aperture around the most intense diffraction spot in the electron diffraction pattern. Up to 5 - 10 seconds was spent on focusing the image in DF, resulting in an additional applied electron fluence of  $0.07 - 0.23\ \text{e}^-/\text{\AA}^2$ . Once the diffraction spot pattern had completely faded, the electron flux was increased to provide enough signal for EDX spectra to be collected from the same region. EDX was used to confirm the presence of FEL by detection of a compositionally characteristic  $\text{Cl-K}\alpha$  X-ray peak at  $2.62\ \text{keV}$ . Ideally spectra were acquired for 30 s live time in order to achieve sufficient signal to noise ratio but in some cases, the increased flux caused the particles to move out of the field of view. This can be due to charging effects and the sample not being fully supported on or adhered to the grid; lowering the signal to noise in the corresponding spectra.

## Conical Dark-Field TEM

Dark field microscopy has previously been used by Ricarte et al. (2015) for the identification of crystalline APIs within formulations.<sup>18</sup> This method allows identification of similarly orientated crystals; however some crystalline regions may be missed because diffraction spots from crystals of the same phase lying at a different orientation are not included in DF image formation.

Conical DF, also known as hollow cone DF, is a method that has previously been used for orientation mapping, defect analysis and grain size measurements in inorganic materials and

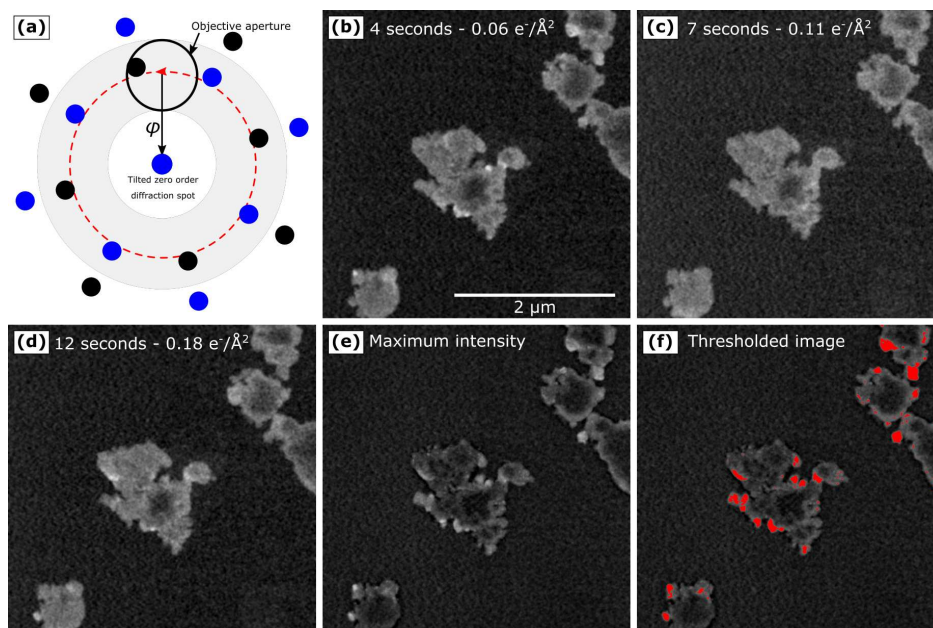


Figure 1: (a) Schematic of a conical DF experiment where an objective aperture is centred around the zero order diffraction spot which is then tilted and precessed around the optical axis. The grey regions shows the areas in the back-focal plane that are sampled and the blue spots represent a diffraction pattern in a different orientation that could be missed when using static DF imaging (b-d) Slices from a conical DF video taken of FEL at different time points. (e) Image showing the maximum pixel intensity across the entire video. (f) Example of thresholding the image to identify areas that are crystalline.

for single particle 3D reconstruction of proteins and identification of inorganic nanoparticles in biological systems.<sup>53–56</sup> Here conical DF is used as a method to overcome the problem in standard DF imaging where only specific diffraction spacings and crystal orientations are sampled. Conical DF increases the contrast between crystalline and amorphous regions, due to precession of the electron beam to sample more areas of reciprocal space. This can provide a higher probability of finding diffraction spots (and therefore different crystals) while still imaging the size and morphology of detected crystalline areas. Figure 1a shows a schematic of the back-focal plane in a conical DF experiment. Here a small objective aperture is centred on the optical axis, the zero-order diffraction beam is then tilted off-axis by an angle  $\varphi$  and the electron beam precessed using the deflection coils to drive the tilted electron beam in a circular path.

Preliminary results using conical DF were generated for crystalline FEL. Figure 1b-d shows different time points collected from a conical DF video. Precession of the electron beam was achieved using the FEI microscope control software and can be carried out by going to the dark field section located within the camera tab. Within this section conical can be selected and the tilt value from the optical axis and precession speed can be easily adjusted. This was set-up prior to imaging. Dark-field mode was then easily recalled and activated by first inserting an objective aperture, centring on the optical axis and then by pressing the DF mode button on the console to recall the settings. The image was focused by manually moving to a sacrificial area nearby and adjusting focus accordingly at an electron flux in the approximate range of  $0.014 - 0.050 \text{ e}^-/(\text{\AA}^2 \text{ s})$ . Slight adjustments to focus were also made if the image started to appear out of focus during acquisition. The intensity of certain areas changes as the electron beam is precessed and different diffraction spots fall within the objective aperture. After an applied electron fluence of approximately  $1.87 \text{ e}^-/\text{\AA}^2$ , we noted that the intensity of these areas had levelled off and dropped to a similar level to that of the surrounding area, indicating the sample has lost crystallinity due to irradiation damage.

The DF video was processed using ImageJ by applying a rolling ball background subtraction (between 10 - 30 pixels) to remove large bright regions that appear due to sample thickness, mainly at the edge of particles. A single image was then generated that showed the maximum intensity for each pixel across the entire data series by using a z-projection to show all areas that were diffracting (Figure 1e). The histogram was then assessed to find the standard deviation ( $\sigma$ ) of the pixel intensity and a threshold of 4 - 6  $\sigma$  was applied. The Rose criterion states that in order for a feature in an image to be detectable, the object intensity must exceed 3 - 5  $\sigma$  above the background pixel values.<sup>57</sup> This provided an outline for identifying where different crystallites were positioned (Figure 1f). In some cases certain areas would visibly change in intensity during the dark field video, indicating crystallinity, however, due to the low total intensity of these diffracting areas they were not always iden-

tified when thresholding. Similarly, areas that appeared bright just due to thickness were identified as crystalline. When these areas were identifiable, the mask was manually adjusted to accordingly into the final image. An example is shown in Figure S1 of the supplementary information.

One limitation of conical DF imaging of these powders is that despite the expected 100% crystallinity of the FEL sample not all particles are shown to contain crystals, even after background subtraction and thresholding (Figure 1f). Crystallites are likely to be present in the central regions of the particles but remain undetected because these regions are too thick to transmit electrons. Almost full crystallinity is confirmed in DF images of thinner particles (Figure S2) and so we acknowledge that these techniques will not detect crystallites in thick regions of ASD powders. We can however use the techniques to detect and investigate crystallinity at the projected edges of particles but even then not all crystals at the particle edges will be identified despite these areas being sufficiently thin for electron transmission. Here, this is due to the FEL crystallites being randomly orientated. Crystals orientated close to or along particular zone axes appear much brighter and are easily identified, however crystals lying in unfavourable orientations for diffraction by the electron beam do not produce strong Bragg spots that fall within the objective aperture. Many transmitted electrons are also incoherently scattered in the thinner regions, increasing the background signal and making the edges of the particles bright relative to the centre. This thickness effect can still be seen in the pure FEL sample (Figure S2) after exposure to a total electron fluence of more than  $3.5 \text{ e}^-/\text{\AA}^2$ , where the majority of the crystals would have been amorphised.

For the solid dispersion samples, a 2.9 mrad semi-angle objective aperture was inserted and aligned on the optical axis and the electron beam was tilted off-axis by 5.5 mrad. The electron beam was then precessed at a frequency of 10 Hz per full rotation. The combination of this diameter objective aperture and beam tilt allows for diffraction spacings between 0.30 nm and 0.96 nm to be sampled. Similar to the crystalline FEL example, a DF video was captured for approximately 10 - 30 seconds as the electron beam was precessed. Where

possible, SAED patterns were then collected by inserting the selected area aperture with a diameter of 1.1  $\mu\text{m}$  at the image plane to further analyse each crystal. Post-acquisition and after processing to threshold, the images were analysed to identify and measure crystallites size.

# Results and Discussion

## Comparison between characterisation techniques

A comparison between the experimentally measured powder X-ray diffraction patterns of crystalline FEL, PVP/VA and the 30:70 w/w FEL-PVP/VA HME solid dispersion shows no sign of crystallinity in the ASD sample (Figure 2). The measured pattern for crystalline FEL shows a number of sharp and distinct peaks most notably at interplanar spacings of: 0.88 nm, 0.80 nm, 0.55 nm, 0.42 nm, 0.39 nm, 0.36 nm, 0.34 nm, 0.33 nm, 0.30 nm and 0.27 nm. These can be indexed to the (011), ( $\bar{1}11$ ), ( $\bar{1}21$ ), ( $\bar{2}21$ ), ( $\bar{3}12$ ), ( $12\bar{3}$ ), ( $22\bar{3}$ ), ( $\bar{3}21$ ), ( $13\bar{3}$ ) and (321) interplanar spacings in FEL form I respectively. The results for the PVP/VA sample exhibit two broad peaks at  $2\theta$  angles of approximately  $12^\circ$  and  $22^\circ$ . Similarly the ASD sample also contains these broad peaks and no characteristic peaks of crystalline FEL were observable in the pattern. Although, we did not carry out pXRD on amorphous FEL other studies have shown that patterns for both amorphous FEL and PVP/VA appear very similar.<sup>13</sup> These results suggest that the form I FEL starting material had transformed into the amorphous form and had been adequately stabilised by intermixing with the PVP/VA at the time of analysis. However, diffraction peaks broaden for crystalline particles of nanometre dimensions, making it difficult for pXRD to differentiate between amorphous and  $<10$  nm, nanocrystalline materials. A more complete and accurate analysis therefore requires the use of complementary characterisation methods.<sup>58,59</sup>

DSC traces examine the thermal events that occur on heating and were collected here as a method to detect evidence of recrystallisation between FEL and PVP/VA. If the sample is crystalline a sharp endothermic peak, indicative of a crystalline solid melting, will be detected upon heating. Whereas, if the sample is amorphous the endothermic peak relating to a crystalline solid melt will be absent and a glass transition ( $T_g$ ) will be observed. The  $T_g$  occurs at a temperature lower than the melt temperature and is evident as a step change from the baseline across a broad range of temperatures due to a change in the specific heat

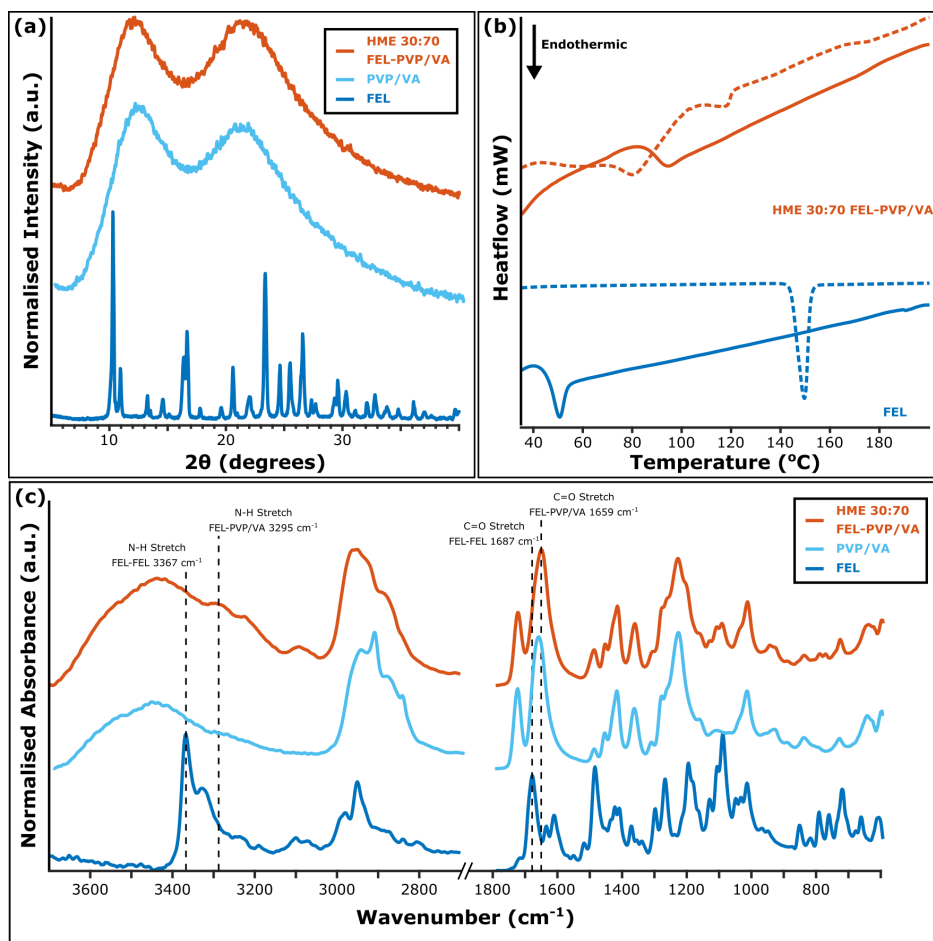


Figure 2: Results for 30:70 FEL-PVP/VA HME solid dispersion, pure FEL and PVP/VA (a) pXRD results showing no signs of crystallinity for the solid dispersion and FEL form I; (b) DSC results for the first cycle (dotted line) and the second cycle (solid line); (c) FTIR results for N-H bond region and C=O bond region.

capacity as an amorphous material transitions from a solid to a super-cooled liquid ( $T_g$  being a second order phase transition). A single  $T_g$  is often used as evidence for the formation of a homogeneously mixed glassy material, while two or more  $T_g$  features are interpreted as a sign of phase separation.<sup>12,60</sup> In the case of ASDs this might correspond to polymer-rich and API-rich domains. However, it has been reported that  $T_g$  does not reliably show API/polymer miscibility as some immiscible blends can exhibit a single  $T_g$  while some miscible blends can show multiple  $T_g$  features. Furthermore, it is challenging for DSC to detect nanoscale domains.<sup>61,62</sup>

Figure 2b shows the DSC traces of the first and second heating cycles for the 30:70 w/w FEL-PVP/VA HME solid dispersion and crystalline FEL. In the first heating cycle for crystalline FEL a strong endothermic peak at 149.7°C is seen, close to the 145°C melting point of FEL form I previously reported by Song et al. (2013).<sup>15</sup> Upon the second heating cycle the melting point at 149.7°C was no longer apparent, indicating a crystalline to amorphous phase transformation. A potential  $T_g$  is visible for the prior-heated FEL and is closely followed by an endothermic event at 49.8°C on the second heating cycle, consistent with a previously reported value for the  $T_g$  of amorphous FEL at around 45°C.<sup>63</sup> In the HME ASD sample a broad endothermic peak is visible at 80°C in the first heating cycle, alongside another peak at 114°C. The first peak observed at 80°C is similar to other studies that have observed broad endothermic peaks at around 80°C due to solvent evaporation.<sup>13</sup> In this case it is possibly due to loss of water vapour that had been absorbed by the polymer, potentially obscuring the  $T_g$ . In the second heating cycle both peaks are no longer visible, indicating that the majority of any absorbed water had been removed from the sample and a  $T_g$  at 88.3°C is evident. The  $T_g$  of a binary system can be calculated using the Gordon-Taylor equation (Equation 2). Here the  $T_g$  of a two-component system is estimated based on the weight fraction ( $w_1$  and  $w_2$ ) of each component and their respective  $T_g$  values, where a value of 45°C was used for the  $T_g$  of FEL.<sup>63</sup> This prediction assumes that the two components are miscible and the free volumes of the components are additive.<sup>64,65</sup>

$$T_{g(mix)} = \frac{w_1 T_{g1} + K w_2 T_{g2}}{w_1 + K w_2} \quad (2)$$

The constant  $K$  is calculated from Equation 3 and the product of the density ( $\rho$ ), and the  $T_g$  of the two components are taken as ratios to calculate  $K$ .

$$K = \frac{T_{g1} \rho_1}{T_{g2} \rho_2} \quad (3)$$

$T_{g(mix)}$  was calculated as 77.0°C for a 30:70 FEL-PVP/VA mixture, using previously

reported values for: the  $T_g$  of PVP/VA measured at 106°C by Patterson et al. (2008); the density of amorphous FEL measured to be 1.33 g/cm<sup>3</sup> by Konno et al. (2006) and the density of PVP/VA measured to be 1.19 g/cm<sup>3</sup> by Six et al. (2004).<sup>10,40,66</sup> The measured  $T_g$  of the mixture deviates positively from the value predicted by the Gordon-Taylor equation by approximately 10°C. Deviations between the calculated and measured  $T_g$  values for different API and polymer mixtures have been previously reported by Patterson et al. (2007).<sup>67-69</sup> They suggest that deviations from the predicted  $T_g$  is compound specific and occurs irrespective of the preparation technique employed.<sup>67</sup> The positive 10°C deviation seen here can be attributed to intermolecular hydrogen bonds between the polymer and API and in the number/strength of these bonds, suggesting a change in stability of the amorphous FEL.<sup>67,69</sup>

Figure 2c shows the IR absorbance spectra plotted against wavenumber between 3700 - 2700 cm<sup>-1</sup> (O-H and N-H region) and 1900 - 600 cm<sup>-1</sup> (C=O region) for crystalline FEL, PVP/VA and the 30:70 w/w FEL-PVP/VA HME ASD. A sharp peak in the crystalline FEL sample can be seen at 3367 cm<sup>-1</sup> indicating a stretch in the N-H bond that has previously been shown to occur at 3370 cm<sup>-1</sup> and 3373 cm<sup>-1</sup> for FEL form I.<sup>40,70</sup> There is also a small broad peak on the shoulder of the N-H stretch in FEL at 3320 cm<sup>-1</sup> which was not assigned to any specific bond vibration and is not observed in other spectra for FEL.

PVP/VA and the HME sample also exhibit a broad absorption band approximately between 3700 - 3100 cm<sup>-1</sup>, which is similar to the O-H stretch that is observed when O-H groups are involved in hydrogen bonding. However, neither FEL nor PVP/VA contain O-H groups. This broad peak may be explained by PVP/VA being hygroscopic, and the absorption bands being a result of latent water that is adsorbed by the polymer (supporting the suggestion of water vapour loss in the first DSC heating cycle of the HME sample; Figure 2b). For the HME solid dispersion sample however, a broad, but weakly absorbing peak can be seen on the shoulder of the O-H band, at approximately 3300 cm<sup>-1</sup>. Other studies have examined the FTIR spectra of amorphous FEL and have reported a broad N-H stretch centred 3340 cm<sup>-1</sup>.<sup>15,40,71,72</sup> It may be that the broad, weak peak observed at 3300

$\text{cm}^{-1}$  in the solid dispersion investigated here is the N-H peak of amorphous FEL red shifted due to hydrogen bond formation with the PVP/VA but without measures at different drug loading and further evidence from other analytical techniques this cannot be confirmed.<sup>15</sup>

In the C=O bond wavenumber range, crystalline FEL has a single peak at  $1687 \text{ cm}^{-1}$ . This peak is due to the C=O stretch from the ester groups and is typically seen between  $1735 - 1750 \text{ cm}^{-1}$  but is red-shifted. In PVP/VA there are two strongly absorbing broad peaks at around  $1732 \text{ cm}^{-1}$  and  $1659 \text{ cm}^{-1}$ , these peaks are derived from the C=O groups in the acetate and pyrrolidone ring structure respectively. Both act as hydrogen bond acceptors, however, the N-H group in FEL should preferentially form hydrogen bonds with the C=O in the pyrrolidone ring due to this being a stronger hydrogen bond acceptor compared to the acetate group.<sup>15,72,73</sup> There is a small red-shift between the solid dispersion and PVP/VA (approximately  $2 - 5 \text{ cm}^{-1}$ ) but, due to the broad absorption peak of PVP/VA in this region, the peak is partially obscured as is consistent with findings of previous studies examining the same drug/polymer system.<sup>15,72,74</sup>

Overall, the bulk techniques provide some measure of the interaction of the FEL with PVP/VA but none indicate the presence of crystalline material within the ASD. TEM however was able to identify 2 different crystalline regions in the 30:70 w/w FEL-PVP/VA solid dispersion, from analysis of a total of 55 areas. This is despite the lack of ability to probe the very centre of large thick particles (as explained in the methods). Figure 3a shows the first region found to be crystalline, identified by a DF image of a small area diffracting near the edge of a milled particle. An electron diffraction pattern of the area was obtained using an electron flux of  $0.023 \text{ e}^-/(\text{\AA}^2 \text{ s})$  (Figure 3b). This flux allowed for 2 - 3 minutes of analysis before the  $C_F$  of FEL had been reached.<sup>29</sup> A systematic row of diffraction spots can be seen in the diffraction pattern with measured d-spacings of  $0.60 \pm 0.01 \text{ nm}$ ,  $0.30 \pm 0.01 \text{ nm}$  and  $0.20 \pm 0.003 \text{ nm}$  that match the (002), (004) and (006) family of planes in FEL form I, respectively. Another row of spots can be seen with measured d-spacings of  $0.19 \pm 0.003 \text{ nm}$ ,  $0.19 \pm 0.003 \text{ nm}$  and  $0.17 \pm 0.002 \text{ nm}$ , corresponding to the  $(62\bar{2})$ ,  $(62\bar{4})$  and  $(62\bar{6})$

planes of FEL form I, respectively. Although this pattern can also be indexed to FEL form III and IV, the match to form I provides the lowest percentage error between the measured d-spacings and angles between spots. A summary of the measured d-spacings and angles are compared to the expected values calculated from the crystal structure in Table 2, alongside the percentage errors.

Figure 3c shows EDX spectra taken from the selected area and from the neighbouring carbon support film. The EDX spectrum from the diffracting area has significant, char-

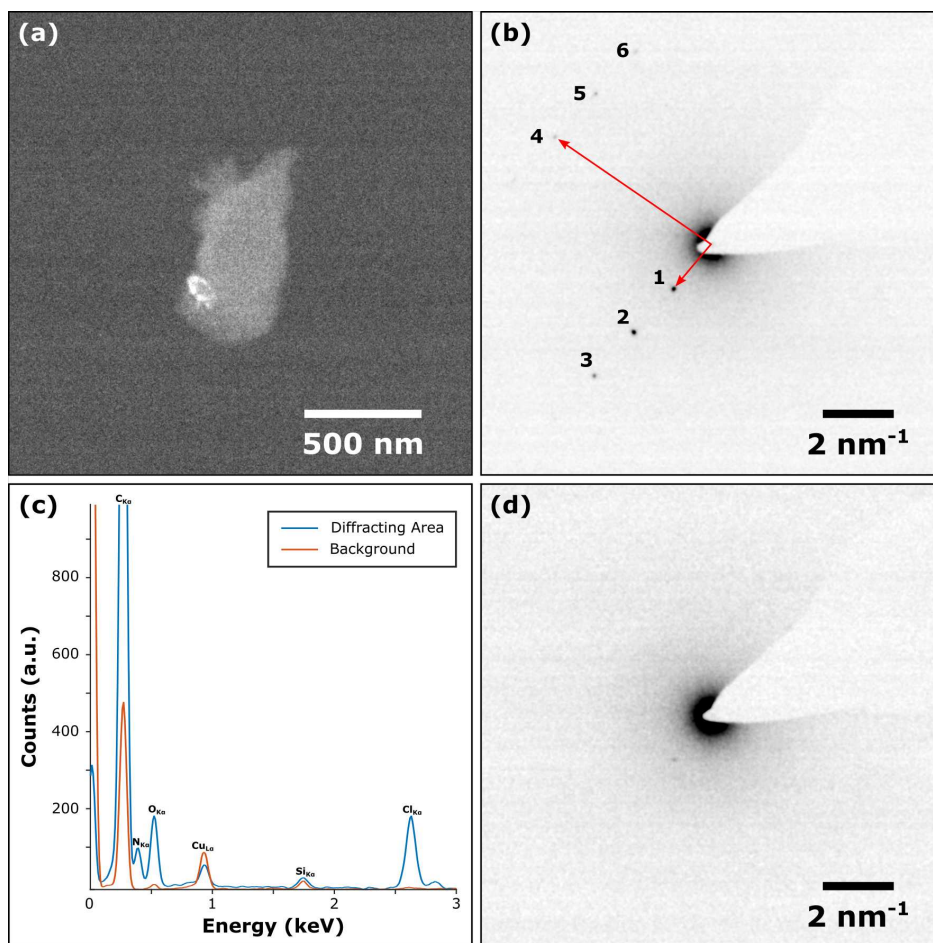


Figure 3: TEM results from one area that appeared crystalline while analysing 30:70 FEL-PVP/VA HME solid dispersion (a) Dark-field TEM image showing diffracting area; (b) Electron diffraction pattern of particle shown in (a), indexable to FEL form I; (c) EDX spectra from the particle showing Cl- $K\alpha$  peak suggesting the presence of FEL compared to the continuous carbon background; (d) Electron diffraction pattern taken from the same area after EDX had been carried out, showing the loss of crystallinity.

Table 2: Measured d-spacings and angles for diffraction spots labelled in Figure 3b compared to possible spacings in FEL form I, III and IV. Average percentage errors between measured and calculated values are equal to  $0.9 \pm 0.01$  %,  $3.4 \pm 0.01$  % and  $3.6 \pm 0.4$  % for form I, III and IV respectively.

Spot	Measured d-spacing (nm)	Calculated d-spacing (nm)			hkl		
		I	III	IV	I	III	IV
1	$0.60 \pm 0.01$	0.60	0.58	0.57	002	$10\bar{3}$	012
2	$0.30 \pm 0.01$	0.30	0.29	0.29	004	$20\bar{6}$	024
3	$0.20 \pm 0.00$	0.20	0.19	0.19	006	309	035
4	$0.19 \pm 0.00$	0.19	0.18	0.18	$62\bar{2}$	$72\bar{1}$	$5\bar{3}1$
5	$0.19 \pm 0.00$	0.19	0.18	0.18	$62\bar{4}$	$62\bar{2}$	$5\bar{4}1$
6	$0.17 \pm 0.00$	0.17	0.16	0.16	$62\bar{6}$	525	553

Angle	Measured angle ( $^{\circ}$ )	Calculated angle ( $^{\circ}$ )			-	-	-
		I	III	IV			
$\theta_{1-4}$	$82.3 \pm 1$	81.6	82.1	81.4	-	-	-
$\theta_{1-5}$	$100.4 \pm 1$	99.6	100.2	99.5	-	-	-
$\theta_{1-6}$	$116.6 \pm 1$	115.9	116.5	115.9	-	-	-

acteristic X-ray peaks for Cl- $K\alpha$  X-rays compared to the background spectrum from the carbon film. Since FEL contains Cl and PVP/VA does not, this supports the identification of FEL in the particle. The diameter of the electron probe was not sufficiently small to accurately determine if the Cl signal is from the crystalline FEL region, the amorphous drug in the particle, or both. Further analysis with a smaller, more focussed electron probe to obtain EDX spectra from across the particle could utilise the ratio of Cl- $K\alpha$  to N- $K\alpha$  X-rays to distinguish between pure crystalline FEL and amorphous FEL intimately mixed with PVP/VA. Figure 4d shows the electron diffraction pattern after acquisition of the EDX spectrum, confirming that the diffraction spots had faded.

## Ageing Study

No sign of crystallinity in the 50:50 w/w FEL-PVP/VA HME solid dispersion was found by pXRD on day 0 (Figure 4). Following one day of ageing, several diffraction peaks began to emerge from the amorphous background, these being the (011), ( $\bar{3}11$ ), ( $12\bar{3}$ ), ( $21\bar{3}$ ), ( $\bar{3}21$ ) and (321) of FEL form I. The intensity of these peaks began to increase on subsequent days (days 2, 4 and 7) and more diffraction peaks of form I FEL became visible ( $\bar{1}11$ ), ( $10\bar{2}$ ),

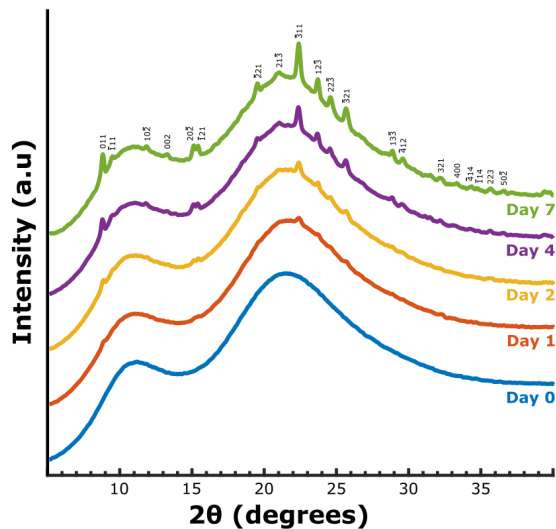


Figure 4: pXRD results for the ageing study for 50:50 FEL-PVP/VA HME solid dispersion stored at 75% relative humidity on days 0, 1, 2, 4 and 7. Each curve has been shifted on the y-axis to create an overlay.

(002), (20 $\bar{2}$ ), ( $\bar{1}21$ ), ( $\bar{2}21$ ), (22 $\bar{3}$ ), (13 $\bar{3}$ ), ( $\bar{4}12$ ), (400), ( $\bar{4}14$ ), ( $\bar{1}14$ ), (223) and (50 $\bar{2}$ ). The amount of crystalline form I was quantified by calculating the % crystalline material for each day and was found to be 0%, 3.2%, 4.8%, 7.3% and 9.6% for days 0, 1, 2, 4 and 7 respectively. No obvious evidence of other polymorphs was present. To calculate the crystal growth rate, a graph of % crystallinity over time was plotted, shown in Figure S3 of the SI. This provided a linear crystal growth rate of 1.56% per day. In addition, Scherrer analysis was used to calculate the average crystallite size assuming a shape factor,  $k$  of 0.94 and negligible instrumental broadening, and this gave an average size of 23.7 nm, 30.7 nm, 31.6 nm and 32.1 nm for days 1, 2, 4 and 7 respectively. A graph of average crystallite size against time is shown in Figure S4 of the SI.

For TEM analysis, fresh samples were prepared from the stored powder for each new measurement to avoid any possible effects caused by damage from the electron beam and to better control the humidity of the analysed sample. Crystallisation was also detected by TEM at the edges of particles during accelerated ageing of the 50:50 w/w FEL-PVP/VA solid dispersion from day 0, where 2 regions out of the 8 examined were found to be crystalline by

Table 3: Measured d-spacings and angles compared to theoretical values for FEL polymorphs for the diffraction pattern shown in Figure 5a. Average percentage errors between measured and theoretical values are equal to  $3.6 \pm 0.4$  and  $1.5 \pm 0.3$ , forms I and II respectively.

Spot	Measured d-spacing (nm)	Calculated d-spacing (nm)		hkl	
		I	II	I	II
1	$0.36 \pm 0.01$	0.38	0.36	$31\bar{1}$	$\bar{3}35$
2	$0.82 \pm 0.02$	0.85	0.81	011	$2\bar{2}0$
3	$0.39 \pm 0.01$	0.40	0.38	$\bar{3}02$	$51\bar{5}$

Angle	Measured angle ( $^{\circ}$ )	Calculated angle ( $^{\circ}$ )		-	-
		I	II		
$\theta_1$	$70 \pm 1$	71	70	-	-
$\theta_2$	$83 \pm 1$	83	84	-	-

SAED. Results from example crystalline areas for each day are shown in Figure 5. Bright field images, conical DF videos, SAED patterns and EDX spectra were all collected on multiple regions that were identified as crystalline by DF TEM on days 0, 1, 2, and 4. No data was collected on day 7 due to technical problems with the equipment.

Figure 5a shows one of these areas from the day 0 sample where a large particle, approximately  $4 \mu\text{m}$  by  $1.5 \mu\text{m}$  is observed. From the SAED pattern, a single crystal can be identified that contains d-spacings of 0.36 nm, 0.82 nm and 0.39 nm, these can be indexed to  $(31\bar{1})$ ,  $(011)$  and  $(\bar{3}02)$  d-spacings in FEL form I. The 0.36 nm, 0.82 nm and 0.39 nm spacings can also be assigned to the hkl values of  $(\bar{3}35)$ ,  $(220)$  and  $(51\bar{5})$  of FEL form II, respectively. A comparison between the measured d-spacings and angles, and the reference crystal structure values are summarised in Table 3 together with the estimated percentage errors and standard deviations. Figure S5 of the SI shows the experimental diffraction pattern overlaid with simulated patterns of FEL form I and II.

After one day of storage, 6 different crystalline regions were found at the edges of particles out of a total of 12 regions that were examined. An example of one of these crystalline regions is shown in Figure 5b, where a BF image indicates where the SAED was placed, a thresholded DF video highlights regions where crystallites were identified, and a corresponding SAED

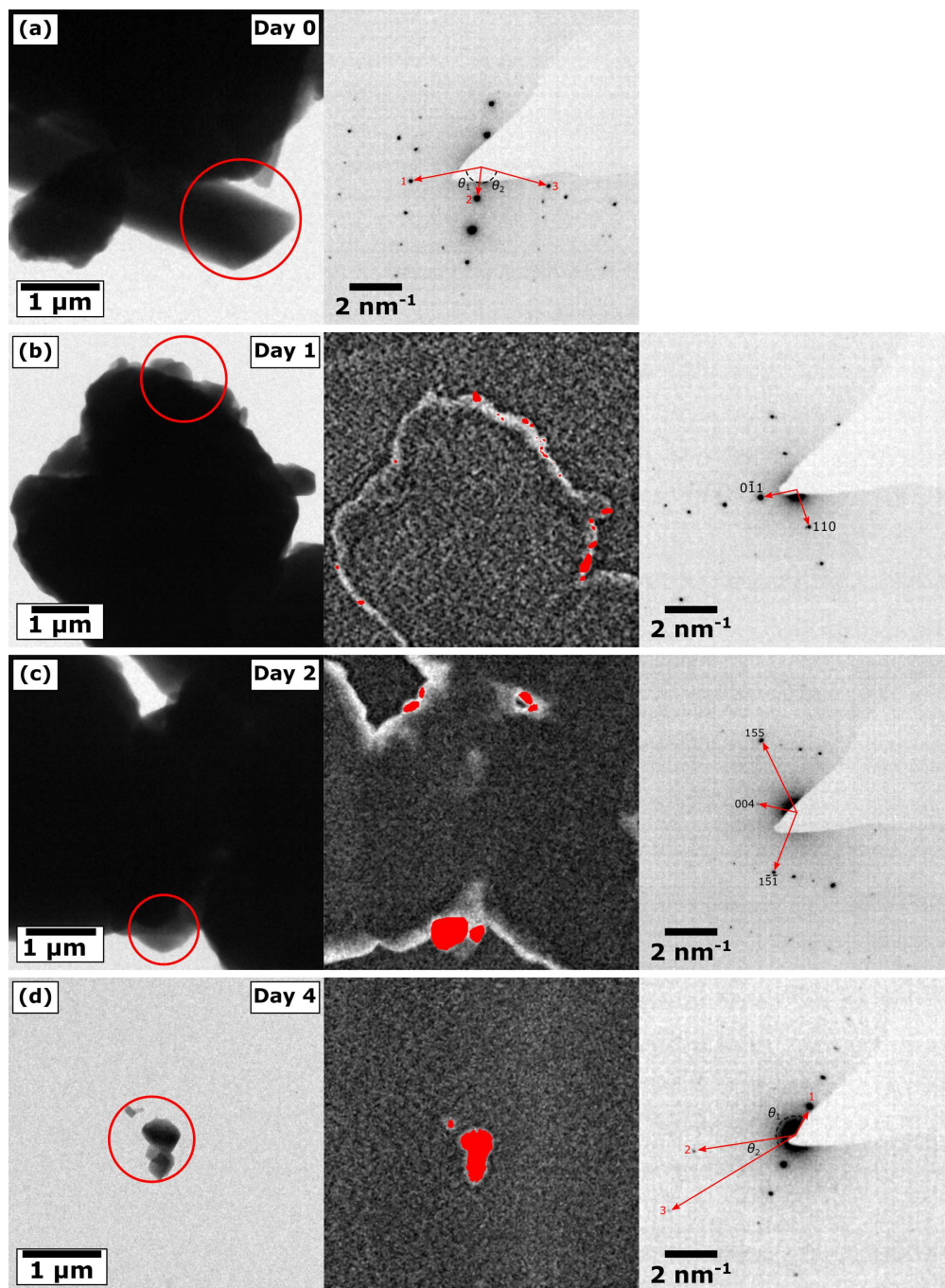


Figure 5: Ageing study TEM results for 50:50 FEL-PVP/VA HME solid dispersion (a) Crystalline area found on day 0 of analysis showing a large FEL crystal, index-able to either form I or II. (b) Crystalline area found on day 1 index-able to FEL form I. (c) Crystalline area found on day 2 index-able to FEL form II. (d) Crystalline area found on day 4 index-able to either FEL form II or IV.

pattern is shown. In this example, the SAED pattern consists of two systematic rows assumed to be part of the same single crystal as well as diffraction spots from several other crystals. These systematic rows could only be indexed to the (110) and (0 $\bar{1}$ 1) hkl values of FEL form I orientated along the  $\langle 111 \rangle$  zone axis, confirming the presence of FEL form I.

After two days of ageing, 8 crystalline regions were identified at the edges of particles from a total of 14 regions that were examined. An example of one of these crystalline regions is shown in Figure 5c. The SAED pattern displays a single crystal that can only be indexed to FEL form II orientated along the  $\langle 510 \rangle$  zone axis, also confirming that FEL form II is present. The BF image shown was acquired at higher electron fluence than the SAED and conical DF video, resulting in the crystalline region decreasing in size compared to the DF image due to increased exposure to additional electrons.

During day 4, 5 crystalline regions were identified from a total of 10 regions that were examined. Figure 5d displays an example of one of the regions analysed that is fully crystalline. The observed d-spacings were measured to be 0.82, nm, 0.25 nm and 0.18 nm for spots 1, 2 and 3 respectively and the angle between spots 1-2 and spots 2-3 to be 123° and 22°. From these measurements the pattern can be indexed to either FEL form I or II, a summary of this comparison is shown in Table 4. All other areas analysed are shown within the SI.

EDX spectra from each area analysed by SAED and shown to be crystalline FEL all produced similar intensity Cl- $K\alpha$  characteristic X-ray peaks at 2.62 keV, supporting the identification of FEL (EDX spectra not shown).

The size of all the crystalline areas found from the DF videos taken during each day of the ageing study were measured by taking the largest dimension of the crystal and plotted on histograms fitted using a log-normal distribution.<sup>75</sup> The median crystallite size (and lower and upper quartiles) were measured to be 80 nm ( $Q_{0.25} = 60$  nm,  $Q_{0.75} = 130$ ), 90 nm ( $Q_{0.25} = 60$  nm,  $Q_{0.75} = 210$ ) and 180 nm ( $Q_{0.25} = 100$  nm,  $Q_{0.75} = 280$ ) on days 1, 2 and 4 of storage at 75% relative humidity respectively. As expected, the data are skewed towards the smaller

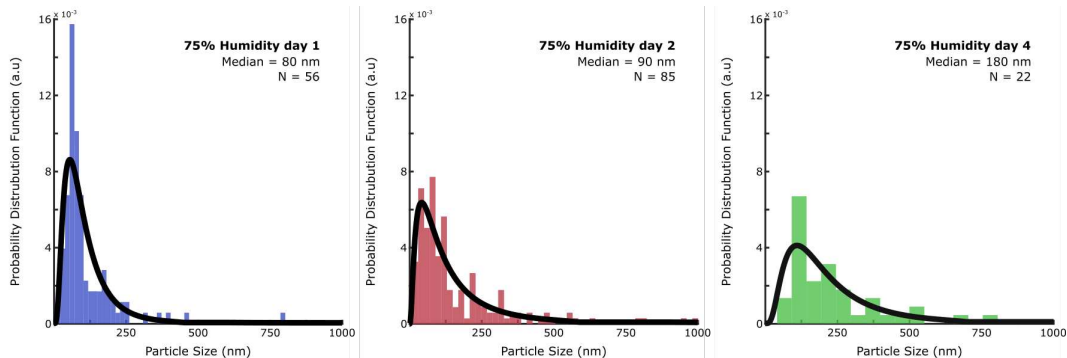


Figure 6: Crystallite size distributions measured from conical DF videos of each area found to be crystalline in the aged 50:50 FEL-PVP/VA HME solid dispersion for day 1, 2 and 4. Fitted using a log normal distribution.

crystallite sizes for all days, as can be seen from Figure 6 and also from the interquartile range between the median and  $q_{0.25}$  being smaller than the interquartile range between  $q_{0.75}$  and the median. The median crystallite size increases with ageing and the upper quartile also increased while the lower quartile either stayed the same or increased only a little. This indicates that the crystalline material is increasing in size over time suggesting crystal growth as well as nucleation is occurring, as indicated by pXRD (Figure 4).

As mentioned early, only sufficiently thin areas that generate an adequate amount of Bragg diffraction are identified as crystalline by DF and conical DF imaging. In addition any

Table 4: Measured d-spacings and angles compared to theoretical values for FEL polymorphs for the diffraction pattern shown in Figure 5d. Average percentage errors between measured and theoretical values are equal to  $1.7 \pm 0.1$  and  $2.4 \pm 0.9$ , forms II and IV respectively.

Spot	Measured d-spacing (nm)	Calculated d-spacing (nm)		hkl	
		II	IV	II	IV
1	$0.82 \pm 0.02$	0.81	0.81	220	110
2	$0.25 \pm 0.00$	0.25	0.25	$\bar{8}\bar{2}\bar{7}$	$\bar{2}\bar{0}\bar{4}$
3	$0.18 \pm 0.00$	0.17	0.17	$\bar{1}\bar{2}\bar{6}\bar{7}$	$\bar{4}\bar{2}\bar{4}$

Angle	Measured angle ( $^{\circ}$ )	Calculated angle ( $^{\circ}$ )		-	-
		II	IV		
$\theta_1$	$123 \pm 1$	123	122	-	-
$\theta_2$	$22 \pm 1$	21	21	-	-

crystals lying in orientations that would not diffract the incident electrons are not detected by these DF techniques. Therefore any crystals within regions too thick for electron transmission or any crystals with a preferred orientation parallel to the electron beam will not be identified. As such, the measured crystallite sizes presented here could be systematically smaller than the true value. However, provided sufficient crystals are sampled and there is no preferred crystal orientation within the particles (that we assume have been randomly deposited on the TEM support film), then the general trend observed here of increasing crystallite size at the edges of ASD particles with aging time should remain valid.

For organic molecules, crystal growth starts to occur when a critical nucleation diameter of typically between 10 and 20 nm is reached.<sup>18</sup> The molecular mobility of solid dispersions is an important factor in both nucleation and growth. The global mobility of API molecules and matrix polymer chains ( $\alpha$ -relaxation of an amorphous material) is directly related to the  $T_g$ .<sup>76-78</sup> The  $T_g$  of the 50:50 FEL-PVP/VA HME solid dispersion was estimated to be 65°C by using the Gordon-Taylor equation. When the sample is stored below the  $T_g$  the global mobility decreases dramatically and the amorphous solid dispersion is generally kinetically stabilised, as should be the case here. However, crystallisation has been observed in systems stored well below  $T_g$ . The cause of this crystallisation is thought to be the occurrence of  $\beta$ -relaxation of polymer chains, which is a localised motion of the chain backbones that have a much lower energy barrier than primary or  $\alpha$ -relaxations of the whole chain. Since the  $T_g$  for FEL-PVP/VA systems are higher than the storage temperature, the start of crystallisation is most likely due to these secondary  $\beta$ -relaxations of the matrix polymer allowing FEL molecules to rearrange and form critical nuclei. Once formed the local concentration of FEL would decrease as the crystal grows and further growth is then limited by the primary polymer  $\alpha$ -relaxation or global mobility. In addition, contaminant particles incorporated during processing such as from the extruder during HME or milling would provide sites for heterogeneous nucleation to occur.<sup>79</sup>

In some cases, only a single polymorph of crystalline FEL could be indexed to an ex-

perimental electron diffraction pattern (for example Figure 5b) and, in others, the pattern could be indexed to multiple polymorphs, due to a limited number of unique d-spacings observed. The percentage error or difference to reference spacings and standard deviation of the error were used to judge which potential polymorph would provide a better match to an observed pattern; where a smaller error and standard deviation of error suggests a better match. Figure 7 shows a bar chart of the possible occurrences for each polymorph that could match the diffraction pattern (within 10% error) and the number of occurrences when a single polymorph provides a significantly better match than another. From this graph, form II appears to occur most frequently in both best match and possible occurrences followed by form I. Forms III and IV match some diffraction patterns better than other polymorphs, however their identity is never uniquely confirmed. In the case of confirmed identities, where only a single polymorph matches, form I is identified three times while form II was identified twice. The confirmed identification of form II and possible identification of forms III and IV by TEM is in distinct contrast to the pXRD results which only identified FEL form I.

Oswalds rule of stages states that the phase that nucleates first tends to be the one with

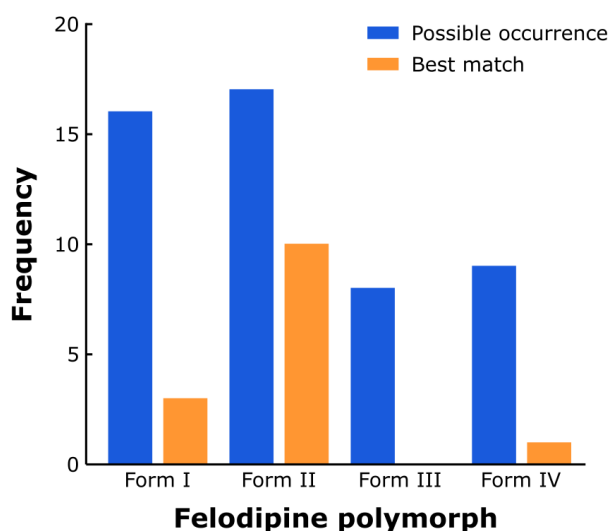


Figure 7: Occurrences of possible FEL polymorphs found and best matches where a single polymorph provides a smaller error/error range than others for crystals detected in the aged 50:50 FEL-PVP/VA HME solid dispersion.

the lowest free-energy barrier of formation and closest Gibbs energy to the initial state rather than the most stable phase overall.<sup>80,81</sup> This suggests that form II may be thermodynamically more favourable to nucleate from the amorphous phase than form I, assuming a similar activation energy barrier needs to be overcome to form the crystal nuclei. The activation energy barrier of nucleation for classical nucleation theory is shown in Equation 4.<sup>82</sup>

$$\Delta G^* = \frac{16\pi\sigma^3}{3\Delta G_v^2} \quad (4)$$

Where  $\Delta G^*$  is the activation energy barrier,  $\Delta G_v$  is the Gibbs energy difference between the amorphous and crystalline phases and  $\sigma$  is the interfacial energy between the crystal-amorphous phase. Larger values of  $\Delta G_v$  relate to a higher tendency for nucleation and increased rate and are always higher for more thermodynamically stable polymorphs. A larger value of  $\sigma$  indicates a higher interfacial energy between the crystal and amorphous phase, increasing the activation energy barrier and lowering the rate of nucleation. Crystal forms where the structure is closer to the amorphous form will have a lower  $\sigma$  value and therefore an increased rate of nucleation. Therefore, form II may have structural or close contact similarities to the stabilised amorphous phase within the ASD, and thus requires less energy to form the correct configuration of molecules. Kinetic drivers such as the addition of atmospheric water can increase the molecular mobility within the polymer matrix and promote rapid crystallisation. Metastable polymorphs tend to form preferentially when crystals are formed quickly compared to slow crystallisation as the latter favours the more thermodynamically stable polymorph.<sup>83,84</sup> Form II is also thought to be a precursor nuclei to form I since both forms are stabilised by similar synthons and both contain similar 1D hydrogen bonding chains between the N-H group and carbonyl group of the methyl ester along the  $\langle 110 \rangle$  zone axis.<sup>85</sup> However, the exact pathway that results in the most stable polymorph forming is unclear, since form I could occur from transitions via multiple polymorphs. Indexable electron diffraction patterns to forms III and IV suggests crystallisation might occur in multiple stages and that form II may be the most kinetically likely of these

since it is identified in a higher number of areas. Alternatively, cross nucleation of polymorphs could result in a mixture of polymorphs. A study examining the crystallisation of nifedipine, an analogue of FEL, from a drug/polymer melt observed the crystal growth of the metastable  $\beta$ -polymorph due to preferential growth from a polymer additive.<sup>86</sup> Other studies have also shown that polymer additives or polymer-rich domains can seed nucleation of a non-equilibrium phase and prevent or slow down simultaneous transformation to the more stable form.<sup>87</sup> Therefore, if phase separation does occur the solid dispersions polymer-rich phases may promote heterogeneous nucleation, lowering the activation energy for metastable polymorphs to form.<sup>88,89</sup>

In some cases where larger particles were sufficiently thin enough for transmission through the whole particle there was a predominance of crystals at the edge of the particle, examples of this can be seen in Figures S17 and S19 of the SI. However, further checks are required to confirm if recrystallisation predominately occurs at the edges of as-deposited powder particles that are currently too thick to transmit electrons through the core of the particle (e.g. those in Figure 5b and c). One potential method to address this would be to resin embed the aged powder and cut ultrathin ( $\sim 100$  nm) sections by ultramicrotome to enable TEM analysis across the entire cross-section of a particle. However, a study by Chen et al. (2018) did report that the surface chemical composition of solid dispersions when exposed to 95% relative humidity, changes from the original 40% drug loading to 69%. This suggests that the addition of water into the binary system causes the hydrophobic drug to move to the solid-air interface creating a non-homogenous dispersion. The concentration of the drug is then high enough at these surfaces to lead to supersaturation and homogeneous nucleation. Surface diffusion is also  $10^6 - 10^7$  times faster than bulk diffusion enabling faster crystal growth at the free surface.<sup>90-92</sup> Previous work by Qi et al. (2011) has studied the crystallisation and phase separation of aged FEL/Eudgrait<sup>®</sup> E PO solid dispersion by ATR-FTIR and various AFM techniques. They identified forms I and II within different sections of the extrudate, with form II mainly found within the cross-section of the 50% drug loading

sample. This was explained by the centre containing higher drug loading (due to thermal expansion of the polymer when leaving the extruder), resulting in homogeneous nucleation of form II. Form I was mainly found at the surfaces of the extrudate and its presence was thought to be due to heterogeneous nucleation from dust particles or particles shed during processing.

Regardless of the nucleation pathway and precise form of the recrystallised FEL in these ASDs, here TEM has been shown to provide a more sensitive measure of recrystallisation in a solid dispersion than conventional bulk techniques such as pXRD. What is also apparent from the above discussion is the extra insight that TEM analysis can bring to a re-crystallised region of a specimen and ultimately this has the potential to be linked to information from other techniques.

This study demonstrates the use of conical DF to identify more crystalline regions compared to static DF imaging or by only using SAED. The corresponding diffractions patterns taken by SAED do however show that the different phases of FEL present after accelerated aging in humid atmospheres can be identified and this provides some insight into the recrystallisation process occurring at particle surfaces during ageing.

Although conical DF imaging by TEM can show areas that are crystalline it is not possible to collect SAED information on every area within the image before damage occurs. One TEM method that may be useful in collecting diffraction information and measuring crystallite size and position in more detail is 4D-STEM. In 4D-STEM, a nm-sized, non-convergent electron probe is scanned across a sample and an electron diffraction pattern collected at each probe position. This technique possesses the ability to use very low electron fluences and has previously been used to examine electron beam sensitive materials such as organic crystals and peptides using an electron fluence of  $1 - 5 \text{ e}^-/\text{\AA}^2$ .<sup>33,34</sup> Using the 4D diffraction dataset, virtual apertures can be applied retrospectively by adding (or subtracting) some subset of the pixels in the diffraction patterns at each probe location to form different bright-field and DF images. This technique has been applied to map the relative orientation, size and

distribution of nanoscale crystalline regions in polymer blends and organic semiconductor molecular thin films.<sup>93,94</sup> In addition, the degree of crystallinity can be calculated by using the ratio between the diffracted and amorphous signals. The underlying nanostructure of theophylline and paracetamol co-crystals have also been analysed using 4D-STEM, identifying a twisted structure within the crystalline rod that may occur perpendicular to the hydrogen bonded planes in the crystal structure.<sup>33</sup> More details and examples of the use of 4D-STEM can be found in a review by Ophus (2019).<sup>95</sup> Overall, further work could be carried out by 4D-STEM on ASD samples to identify and quantify any crystalline regions present within a sample. In addition it could provide information on crystallite location, size and polymorphs that are present, and reveal information on the underlying nanostructure or matrix polymer phase separation.

## Conclusion

In this study, TEM was more successful at identifying signs of crystallisation in an amorphous solid dispersion of FEL and PVP/VA prepared by hot-melt extrusion (30/70 w/w) than either pXRD, FTIR or DSC. Suggesting TEM has a better limit of detection compared to these techniques. However, it is difficult to provide a fully quantitative assessment by TEM of the amount of crystallisation occurring because of the limited sampling possible across thick particles and in the time or dose available to analyse the drug before the crystal structure becomes damaged by the electron beam.

TEM has also been shown to provide some insights into the recrystallisation process of a similar solid dispersion (50/50 w/w) during accelerated ageing conditions in humid atmospheres by detecting the presence of multiple polymorphs of FEL at the surfaces of aged particles. Form II and the stable form I of FEL were both conclusively identified by TEM. Conical dark field imaging with suitable image processing was useful in both identifying crystals and for measuring the particle/crystallite area, although the sizes could have been systematically underestimated because any crystallinity in the core of particles too thick for electron transmission could not be assessed. The size distribution of crystalline regions detected at the projected edges or surfaces of particles increased over time, consistent with the increase in the fraction of crystalline material measured by pXRD. TEM also suggested that nucleation and growth of recrystallisation occurs at surfaces of ASD particles, as might be expected for a water-induced transformation.

Further development in TEM techniques could provide more information regarding nanostructure, size and position of crystallites, local degree of crystallinity and polymorphic information in ASDs, at a limit of detection significantly lower than for pXRD, FTIR and DSC. Insight into crystallisation pathways will enable different strategies to be developed to control and prevent occurrence of both crystallisation and unwanted crystalline forms. Overall the sensitivity to detection of crystallinity shown here by TEM could enable shorter real-time stability studies of ASDs with richer insight into transformation processes, leading

to faster product development and therefore better outcomes for patients.

## Acknowledgement

The authors gratefully acknowledge financial support by the EPSRC (Award number 1505716), and funding from AstraZeneca is acknowledged.

## Supporting Information Available

The Supporting Information is available online.

S1 Example of manually edited mask and automatic in ImageJ.

S2 Conical-DF of felodipine at selected frames.

S3 Graph of percentage crystallinity overtime measured from pXRD.

S4 Graph of average crystallite size overtime measured from pXRD.

S5-22 Figures of all crystalline regions identified during the ageing study.

Tables of measured/calculated d-spacings and angles for potential forms of felodipine that match (Table S1 - 11).

## References

- (1) Loftsson, T.; Brewster, M. E. Pharmaceutical applications of cyclodextrins: basic science and product development. *Journal of Pharmacy and Pharmacology* **2010**, *62*, 1607–1621.
- (2) Kanaujia, P.; Poovizhi, P.; Ng, W.; Tan, R. Amorphous formulations for dissolution and bioavailability enhancement of poorly soluble APIs. *Powder Technology* **2015**, *285*, 2–15.
- (3) Khadka, P.; Ro, J.; Kim, H.; Kim, I.; Kim, J. T.; Kim, H.; Cho, J. M.; Yun, G.; Lee, J. Pharmaceutical particle technologies: An approach to improve drug solubility,

- dissolution and bioavailability. *Asian Journal of Pharmaceutical Sciences* **2014**, *9*, 304–316.
- (4) Sareen, S.; Mathew, G.; Joseph, L. Improvement in solubility of poor water-soluble drugs by solid dispersion. *International Journal of Pharmaceutical Investigation* **2012**, *2*, 12–17.
- (5) Cabral, H.; Kataoka, K. Progress of drug-loaded polymeric micelles into clinical studies. *Journal of Controlled Release* **2014**, *190*, 465–476.
- (6) Gao, L.; Liu, G.; Ma, J.; Wang, X.; Zhou, L.; Li, X.; Wang, F. Application of Drug Nanocrystal Technologies on Oral Drug Delivery of Poorly Soluble Drugs. *Pharmaceutical Research* **2013**, *30*, 307–324.
- (7) Jermain, S. V.; Brough, C.; Williams, R. O. Amorphous solid dispersions and nanocrystal technologies for poorly water-soluble drug delivery An update. *International Journal of Pharmaceutics* **2018**, *535*, 379–392.
- (8) Leuner, C.; Dressman, J. Improving drug solubility for oral delivery using solid dispersions. *European Journal of Pharmaceutics and Biopharmaceutics* **2000**, *50*, 47–60.
- (9) Yamashita, K.; Nakate, T.; Okimoto, K.; Ohike, A.; Tokunaga, Y.; Ibuki, R.; Higaki, K.; Kimura, T. Establishment of new preparation method for solid dispersion formulation of tacrolimus. *International Journal of Pharmaceutics* **2003**, *267*, 79–91.
- (10) Six, K.; Verreck, G.; Peeters, J.; Brewster, M.; Mooter, G. V. d. Increased physical stability and improved dissolution properties of itraconazole, a class II drug, by solid dispersions that combine fast- and slow-dissolving polymers. *Journal of Pharmaceutical Sciences* **2004**, *93*, 124–131.
- (11) Taylor, L. S.; Zhang, G. G. Physical chemistry of supersaturated solutions and im-

- plications for oral absorption. *Advanced Drug Delivery Reviews* **2016**, *101*, 122–142, Understanding the challenges of beyond-rule-of-5 compounds.
- (12) Baird, J. A.; Taylor, L. S. Evaluation of amorphous solid dispersion properties using thermal analysis techniques. *Advanced Drug Delivery Reviews* **2012**, *64*, 396–421.
- (13) Ivanisevic, I. Physical stability studies of miscible amorphous solid dispersions. *Journal of Pharmaceutical Sciences* **2010**, *99*, 4005–4012.
- (14) Que, C.; Gao, Y.; Raina, S. A.; Zhang, G. G. Z.; Taylor, L. S. Paclitaxel Crystal Seeds with Different Intrinsic Properties and Their Impact on Dissolution of Paclitaxel-HPMCAS Amorphous Solid Dispersions. *Crystal Growth & Design* **2018**, *18*, 1548–1559.
- (15) Song, Y.; Wang, L.; Yang, P.; Wenslow, R. M.; Tan, B.; Zhang, H.; Deng, Z. Physicochemical Characterization of Felodipine-Kollidon VA64 Amorphous Solid Dispersions Prepared by Hot-Melt Extrusion. *Journal of Pharmaceutical Sciences* **2013**, *102*, 1915–1923.
- (16) Thakral, N. K.; Zanon, R. L.; Kelly, R. C.; Thakral, S. Applications of Powder X-Ray Diffraction in Small Molecule Pharmaceuticals: Achievements and Aspirations. *Journal of Pharmaceutical Sciences* **2018**, *107*, 2969 – 2982.
- (17) Dedroog, S.; Huygens, C.; Van den Mooter, G. Chemically identical but physically different: A comparison of spray drying, hot melt extrusion and cryo-milling for the formulation of high drug loaded amorphous solid dispersions of naproxen. *European Journal of Pharmaceutics and Biopharmaceutics* **2019**, *135*, 1 – 12.
- (18) Ricarte, R. G.; Lodge, T. P.; Hillmyer, M. A. Detection of Pharmaceutical Drug Crystallites in Solid Dispersions by Transmission Electron Microscopy. *Drug Development and Industrial Pharmacy* **2015**, *12*, 983–990.

- (19) Moseson, D. E.; Mugheirbi, N. A.; Stewart, A. A.; Taylor, L. S. Nanometer-Scale Residual Crystals in a Hot Melt Extruded Amorphous Solid Dispersion: Characterization by Transmission Electron Microscopy. *Crystal Growth & Design* **2018**, *18*, 7633–7640.
- (20) Moseson, D. E.; Parker, A. S.; Beaudoin, S. P.; Taylor, L. S. Amorphous solid dispersions containing residual crystallinity: Influence of seed properties and polymer adsorption on dissolution performance. *European Journal of Pharmaceutical Sciences* **2020**, *146*, 105276.
- (21) Li, N.; Gilpin, C. J.; Taylor, L. S. Understanding the Impact of Water on the Miscibility and Microstructure of Amorphous Solid Dispersions: An AFM-LCR and TEM-EDX Study. *Molecular Pharmaceutics* **2017**, *14*, 1691–1705.
- (22) Ricarte, R. G.; Lodge, T. P.; Hillmyer, M. A. Nanoscale Concentration Quantification of Pharmaceutical Actives in Amorphous Polymer Matrices by Electron Energy-Loss Spectroscopy. *Langmuir* **2016**, *32*, 7411–7419.
- (23) Stenn, K.; Bahr, G. Specimen damage caused by the beam of the transmission electron microscope, a correlative reconsideration. *Journal of Ultrastructure Research* **1970**, *31*, 526–550.
- (24) Egerton, R. F.; Li, P.; Malac, M. Radiation damage in the TEM and SEM. *Micron* **2004**, *35*, 399–409.
- (25) Egerton, R. F. Control of radiation damage in the TEM. *Ultramicroscopy* **2013**, *127*, 100–108.
- (26) Egerton, R. Radiation damage to organic and inorganic specimens in the TEM. *Micron* **2019**, *119*, 72–87.
- (27) Jones, W.; Thomas, J. M. Application of electron microscopy to organic solid-state chemistry. *Progress in Solid State Chemistry* **1979**, *12*, 101–124.

- (28) Henderson, R.; Glaeser, R. M. Quantitative analysis of image contrast in electron micrographs of beam-sensitive crystals. *Ultramicroscopy* **1985**, *16*, 139–150.
- (29) S'ari, M.; Blade, H.; Brydson, R.; Cosgrove, S.; Hondow, N.; Hughes, L.; Brown, A. Toward Developing a Predictive Approach To Assess Electron Beam Instability during Transmission Electron Microscopy of Drug Molecules. *Molecular Pharmaceutics* **2018**, *15*, 5114–5123.
- (30) Das, P. P.; Guzzinati, G.; Coll, C.; Gomez Perez, A.; Nicolopoulos, S.; Estrade, S.; Peiro, F.; Verbeeck, J.; Zompra, A. A.; Galanis, A. S. Reliable Characterization of Organic & Pharmaceutical Compounds with High Resolution Monochromated EEL Spectroscopy. *Polymers* **2020**, *12*.
- (31) S'ari, M.; Cattle, J.; Hondow, N.; Brydson, R.; Brown, A. Low dose scanning transmission electron microscopy of organic crystals by scanning moiré fringes. *Micron* **2019**, *120*, 1–9.
- (32) S'ari, M.; Koniuch, N.; Brydson, R.; Hondow, N.; Brown, A. High-resolution imaging of organic pharmaceutical crystals by transmission electron microscopy and scanning moiré fringes. *Journal of Microscopy* *279*, 197–206.
- (33) Johnstone, D. N.; Allen, C. S.; Danaie, M.; Copley, R. C.; Brum, J.; Kirkland, A. I.; Midgley, P. A. Low-Dose Scanning Electron Diffraction Microscopy of Mechanochemically Nanostructured Pharmaceuticals. *Microscopy and Microanalysis* **2019**, *25*, 1746–1747.
- (34) Gallagher-Jones, M.; Ophus, C.; Bustillo, K. C.; Boyer, D. R.; Panova, O.; Glynn, C.; Zee, C.-T.; Ciston, J.; Mancina, K. C.; Minor, A. M.; Rodriguez, J. A. Nanoscale mosaicity revealed in peptide microcrystals by scanning electron nanodiffraction. *Communications Biology* **2019**, *2*.

- (35) Anderberg, E.; Bisrat, M.; Nyström, C. Physicochemical aspects of drug release. VII. The effect of surfactant concentration and drug particle size on solubility and dissolution rate of felodipine, a sparingly soluble drug. *International Journal of Pharmaceutics* **1988**, *47*, 67–77.
- (36) Fu, J.; Cui, L.; Yang, C.; Xiong, H.; Ren, G.; Ma, X.; Jing, Q.; Fuzheng, R. Screen for Inhibitors of Crystal Growth to Identify Desirable Carriers for Amorphous Solid Dispersions Containing Felodipine. *AAPS PharmSciTech* **2018**, *19*, 1231–1242.
- (37) Karavas, E.; Georgarakis, E.; Sigalas, M. P.; Avgoustakis, K.; Bikiaris, D. Investigation of the release mechanism of a sparingly water-soluble drug from solid dispersions in hydrophilic carriers based on physical state of drug, particle size distribution and drug-polymer interactions. *European Journal of Pharmaceutics and Biopharmaceutics* **2007**, *66*, 334–347.
- (38) Karavas, E.; Ktistis, G.; Xenakis, A.; Georgarakis, E. Effect of hydrogen bonding interactions on the release mechanism of felodipine from nanodispersions with polyvinylpyrrolidone. *European Journal of Pharmaceutics and Biopharmaceutics* **2006**, *63*, 103–114.
- (39) Konno, H.; Handa, T.; Alonzo, D. E.; Taylor, L. S. Effect of polymer type on the dissolution profile of amorphous solid dispersions containing felodipine. *European Journal of Pharmaceutics and Biopharmaceutics* **2008**, *70*, 493–499.
- (40) Konno, H.; Taylor, L. S. Influence of different polymers on the crystallization tendency of molecularly dispersed amorphous felodipine. *Journal of Pharmaceutical Sciences* **2006**, *95*, 2692–2705.
- (41) Mahmah, O.; Tabbakh, R.; Kelly, A.; Paradkar, A. A comparative study of the effect of spray drying and hot-melt extrusion on the properties of amorphous solid dispersions containing felodipine. *Journal of Pharmacy and Pharmacology* **2014**, *66*, 275–284.

- (42) Marsac, P. J.; Konno, H.; Rumondor, A. C. F.; Taylor, L. S. Recrystallization of Nifedipine and Felodipine from Amorphous Molecular Level Solid Dispersions Containing Poly(vinylpyrrolidone) and Sorbed Water. *Pharmaceutical Research* **2008**, *25*, 647–656.
- (43) Marsac, P. J.; Konno, H.; Taylor, L. S. A Comparison of the Physical Stability of Amorphous Felodipine and Nifedipine Systems. *Pharmaceutical Research* **2006**, *23*, 2306–2316.
- (44) Nollenberger, K.; Gryczke, A.; Meier, C.; Dressman, J.; Schmidt, M.; Brhne, S. Pair distribution function X-ray analysis explains dissolution characteristics of felodipine melt extrusion products. *Journal of Pharmaceutical Sciences* **2009**, *98*, 1476–1486.
- (45) Rumondor, A. C. F.; Stanford, L. A.; Taylor, L. S. Effects of Polymer Type and Storage Relative Humidity on the Kinetics of Felodipine Crystallization from Amorphous Solid Dispersions. *Pharmaceutical Research* **2009**, *26*, 2599–2606.
- (46) Surov, A. O.; Solanko, K. A.; Bond, A. D.; Perlovich, G. L.; Bauer-Brandl, A. Crystallization and Polymorphism of Felodipine. *Crystal Growth and Design* **2012**, *12*, 4022–4030.
- (47) Wang, L.; Song, Y.; Yang, P.; Tan, B.; Zhang, H.; Deng, Z. Preparation and thermodynamic properties of Felodipine form IV. *Journal of Thermal Analysis and Calorimetry* **2015**, *120*, 947–951.
- (48) Nurzyska, K.; Booth, J.; Roberts, C. J.; McCabe, J.; Dryden, I.; Fischer, P. M. Long-Term Amorphous Drug Stability Predictions Using Easily Calculated, Predicted, and Measured Parameters. *Molecular Pharmaceutics* **2015**, *12*, 3389–3398.
- (49) Luebbert, C.; Sadowski, G. Moisture-induced phase separation and recrystallization in amorphous solid dispersions. *International Journal of Pharmaceutics* **2017**, *532*, 635–646.

- (50) Greenspan, L. Humidity Fixed Points of Binary Saturated Aqueous Solutions. *Journal of Research of the National Bureau of Standards Section A: Physics and Chemistry* **1977**, *81A*.
- (51) Rumondor, A. C.; Taylor, L. S. Application of Partial Least-Squares (PLS) modeling in quantifying drug crystallinity in amorphous solid dispersions. *International Journal of Pharmaceutics* **2010**, *398*, 155–160.
- (52) Shah, B.; Kakumanu, V. K.; Bansa, A. K. Analytical techniques for quantification of amorphous/crystalline phases in pharmaceutical solids. *Journal of Pharmaceutical Sciences* **2006**, *95*, 1641–1665.
- (53) Yao, B.; Sun, T.; Warren, A.; Heinrich, H.; Barmak, K.; Coffey, K. R. High contrast hollow-cone dark field transmission electron microscopy for nanocrystalline grain size quantification. *Micron* **2010**, *41*, 177–182.
- (54) Wu, G.; Zaefferer, S. Advances in TEM orientation microscopy by combination of dark-field conical scanning and improved image matching. *Ultramicroscopy* **2009**, *109*, 1317–1325.
- (55) Klein, N. D.; Hurley, K. R.; Feng, Z. V.; Haynes, C. L. Dark Field Transmission Electron Microscopy as a Tool for Identifying Inorganic Nanoparticles in Biological Matrices. *Analytical Chemistry* **2015**, *87*, 4356–4362.
- (56) Tsai, C.-Y.; Chang, Y.-C.; Lobato, I.; Van Dyck, D.; Chen, F.-R. Hollow Cone Electron Imaging for Single Particle 3D Reconstruction of Proteins. *Scientific Reports* **2016**, *6*.
- (57) Rose, A. *Vision: Human and Electronic*, 1st ed.; Springer US, 1973.
- (58) Yu, L. Amorphous pharmaceutical solids: preparation, characterization and stabilization. *Advanced Drug Delivery Reviews* **2001**, *48*, 27–42.

- (59) Johari, G.; Ram, S.; Astl, G.; Mayer, E. Characterizing amorphous and microcrystalline solids by calorimetry. *Journal of Non-Crystalline Solids* **1990**, *116*, 282–285.
- (60) Karavas, E.; Ktistis, G.; Xenakis, A.; Georgarakis, E. Miscibility Behavior and Formation Mechanism of Stabilized Felodipine-Polyvinylpyrrolidone Amorphous Solid Dispersions. *Drug Development and Industrial Pharmacy* **2005**, *31*, 473–489.
- (61) Lodge, T.; Wood, E.; Haley, J. Two Calorimetric Glass Transitions Do Not Necessarily Indicate Immiscibility: The Case of PEO/PMMA. *J. Polym. Sci., Part B: Polym. Phys.* **2006**, *44*, 756–763.
- (62) Qian, F.; Huang, J.; Zhu, Q.; Haddadin, R.; Gawel, J.; Garmise, R.; Hussain, M. Is a distinctive single T<sub>g</sub> a reliable indicator for the homogeneity of amorphous solid dispersion? *International Journal of Pharmaceutics* **2010**, *395*, 232–235.
- (63) Kerc, J.; Srcic, S.; Mohar, M.; mid Korbar, J. S. Some physicochemical properties of glassy felodipine. *International Journal of Pharmaceutics* **1991**, *68*, 25–33.
- (64) Gordon, M.; Taylor, J. S. Ideal copolymers and the secondorder transitions of synthetic rubbers. i. noncrystalline copolymers. *Journal of Applied Chemistry* **1952**, *2*, 493–500.
- (65) Simha, R.; Boyer, R. F. On a General Relation Involving the Glass Temperature and Coefficients of Expansion of Polymers. *The Journal of Chemical Physics* **1962**, *37*, 1003–1007.
- (66) Patterson, J. E.; James, M. B.; Forster, A. H.; Rades, T. Melt Extrusion and Spray Drying of Carbamazepine and Dipyridamole with Polyvinylpyrrolidone/Vinyl Acetate Copolymers. *Drug Development and Industrial Pharmacy* **2008**, *34*, 95–106.
- (67) Patterson, J. E.; James, M. B.; Forster, A. H.; Lancaster, R. W.; Butler, J. M.; Rades, T. Preparation of glass solutions of three poorly water soluble drugs by spray drying, melt extrusion and ball milling. *International Journal of Pharmaceutics* **2007**, *336*, 22–34.

- (68) Forster, A.; Hempenstall, J.; Tucker, I.; Rades, T. Selection of excipients for melt extrusion with two poorly water-soluble drugs by solubility parameter calculation and thermal analysis. *International Journal of Pharmaceutics* **2001**, *226*, 147–161.
- (69) Taylor, L. S.; Zografi, G. Sugar-polymer hydrogen bond interactions in lyophilized amorphous mixtures. *Journal of Pharmaceutical Sciences* **1998**, *87*, 1615–1621.
- (70) Pandey, M. M.; Jaipal, A.; Charde, S. Y.; Goel, P.; Kumar, L. Application of mid-IR spectroscopy for the characterization of pharmaceutical systems. *Pharmaceutical Development and Technology* **2016**, *21*, 463–474.
- (71) Tang, X. C.; Pikal, M. J.; Taylor, L. S. A Spectroscopic Investigation of Hydrogen Bond Patterns in Crystalline and Amorphous Phases in Dihydropyridine Calcium Channel Blockers. *Pharmaceutical Research* **2002**, *19*, 477–483.
- (72) Kestur, U. S.; Taylor, L. S. Role of polymer chemistry in influencing crystal growth rates from amorphous felodipine. *CrystEngComm* **2010**, *12*, 2390–2397.
- (73) Taylor, L. S.; Langkilde, F. W.; Zografi, G. Fourier transform Raman spectroscopic study of the interaction of water vapor with amorphous polymers. *Journal of Pharmaceutical Sciences* **2001**, *90*, 888–901.
- (74) Karavas, E.; Ktistis, G.; Xenakis, A.; Georgarakis, E. Miscibility Behavior and Formation Mechanism of Stabilized Felodipine-Polyvinylpyrrolidone Amorphous Solid Dispersions. *Drug Development and Industrial Pharmacy* **2008**, *31*, 473–489.
- (75) Ungár, T.; Gubicza, J.; Ribárik, G.; Borbély, A. Crystallite size distribution and dislocation structure determined by diffraction profile analysis: principles and practical application to cubic and hexagonal crystals. *Journal of Applied Crystallography* **2001**, *34*, 298–310.

- (76) Ke, P.; Hasegawa, S.; Al-Obaidi, H.; Buckton, G. Investigation of preparation methods on surface/bulk structural relaxation and glass fragility of amorphous solid dispersions. *International journal of pharmaceutics* **2012**, *422*, 170–178.
- (77) Meng, F.; Gala, U.; Chauhan, H. Classification of solid dispersions: correlation to (i) stability and solubility (ii) preparation and characterization techniques. *Drug Development and Industrial Pharmacy* **2015**, *41*, 1401–1415.
- (78) Huang, S.; Williams, R. O. Effects of the Preparation Process on the Properties of Amorphous Solid Dispersions. *AAPS PharmSciTech* **2018**, *19*, 1971–1984.
- (79) Qi, S.; Belton, P.; Nollenberger, K.; Gryczke, A.; Craig, D. Q. M. Compositional Analysis of Low Quantities of Phase Separation in Hot-Melt-Extruded Solid Dispersions: A Combined Atomic Force Microscopy, Photothermal Fourier-Transform Infrared Microspectroscopy, and Localised Thermal Analysis Approach. *Pharmaceutical Research* **2011**, *28*, 2311–2326.
- (80) Stranski, I. N.; Totomanow, D. Nucleation rate and Ostwald step rule. *Journal of Physical Chemistry* **1933**, *162A*.
- (81) Turnbull, D. Metastable structures in metallurgy. *Metallurgical Transactions B* **1981**, *12*, 217–230.
- (82) Turnbull, D.; Fisher, J. C. Rate of Nucleation in Condensed Systems. *The Journal of Chemical Physics* **1949**, *17*, 71–73.
- (83) Lee, A. Y.; Erdemir, D.; Myerson, A. S. Crystal Polymorphism in Chemical Process Development. *Annual Review of Chemical and Biomolecular Engineering* **2011**, *2*, 259–280.
- (84) Duong, T. V.; Ludeke, D.; Bockstal, P.-J. V.; Beer, T. D.; Humbeeck, J. V.; den

- Mooter, G. V. Polymorphism of Indomethacin in Semicrystalline Dispersions: Formation, Transformation, and Segregation. *Molecular Pharmaceutics* **2018**, *15*, 1037–1051.
- (85) Lou, B.; Boström, D.; Velaga, S. P. Polymorph Control of Felodipine Form II in an Attempted Cocrystallization. *Crystal Growth & Design* **2009**, *9*, 1254–1257.
- (86) Gunn, E.; Guzei, I. A.; Cai, T.; Yu, L. Polymorphism of Nifedipine: Crystal Structure and Reversible Transition of the Metastable Polymorph. *Crystal Growth & Design* **2012**, *12*, 2037–2043.
- (87) Tao, J.; Yu, L. Kinetics of Cross-Nucleation between Polymorphs. *The Journal of Physical Chemistry B* **2006**, *110*, 7098–7101.
- (88) Frank, D. S.; Matzger, A. J. Probing the Interplay between Amorphous Solid Dispersion Stability and Polymer Functionality. *Molecular Pharmaceutics* **2018**, *15*, 2714–2720.
- (89) Frank, D. S.; Matzger, A. J. Influence of Chemical Functionality on the Rate of Polymer-Induced Heteronucleation. *Crystal Growth & Design* **2017**, *17*, 4056–4059.
- (90) Cai, T.; Zhu, L.; Yu, L. Crystallization of Organic Glasses: Effects of Polymer Additives on Bulk and Surface Crystal Growth in Amorphous Nifedipine. *Pharmaceutical Research* **2011**, *28*, 2458–2466.
- (91) Ishida, H.; Wu, T.; Yu, L. Sudden Rise of Crystal Growth Rate of Nifedipine near  $T_g$  without and with Polyvinylpyrrolidone. *Journal of Pharmaceutical Sciences* **2007**, *96*, 1131–1138.
- (92) Yu, L. Surface mobility of molecular glasses and its importance in physical stability. *Advanced Drug Delivery Reviews* **2016**, *100*, 3–9.
- (93) Panova, O.; Chen, X. C.; Bustillo, K. C.; Ophus, C.; Bhatt, M. P.; Balsara, N.; Minor, A. M. Orientation mapping of semicrystalline polymers using scanning electron nanobeam diffraction. *Micron* **2016**, *88*, 30–36.

- (94) Panova, O.; Ophus, C.; Takacs, C. J.; Bustillo, K. C.; Balhorn, L.; Salleo, A.; Balsara, N.; Minor, A. M. Diffraction imaging of nanocrystalline structures in organic semiconductor molecular thin films. *Nature Materials* **2019**, *18*, 860–865.
- (95) Ophus, C. Four-Dimensional Scanning Transmission Electron Microscopy (4D-STEM): From Scanning Nanodiffraction to Ptychography and Beyond. *Microscopy and Microanalysis* **2019**, *25*, 563–582.

# Graphical TOC Entry

